

Energy flux as a tool in locating tsunami secondary sources

Kowalik Zygmunt

Institute Marine Science, School of Fishery and Ocean Science, University of Alaska Fairbanks

Email:ffzk@ims.uaf.edu

Abstract

The sea levels recorded in the wake of Indian Ocean Tsunami of December 2004 and of the Kuril Island Tsunami of November 2006 show strong tsunami signal enhancement of the late arriving secondary waves. Using these tsunami events we demonstrate that sudden changes caused by higher energy pulses in the intermittent tsunami wave trains can be assessed by energy fluxes. Therefore, to delineate the regions of tsunami wave amplification and travel time we propose to use energy flux.

A series of numerical experiments defined in explicit way the bathymetric features which scatter tsunami signal towards ports, like Crescent City. Identification of the distant bathymetric features was achievable since the energy flux vector delineated the energy pathways that coupled distant bathymetric features to ports located thousands of kilometers apart. Calculations of the energy flux vector involves simple formulas based on two components of velocity and sea level. The maximum of the energy flux (which has no directional properties) can be evaluated from the sea level amplitude, hence both observed and computed sea level can be used for this purpose. The main task of this paper is to suggest that tsunami warning and prediction services should use numerical-hydrodynamical models with wider scope of physical processes by incorporating the energy balance equation into presently used tools.

Introduction

Along with the primary source of tsunami, sea level uplift due to earthquake, secondary sources due to scattering and refocusing, complicate the process of tsunami propagation. As amplified tsunami signals along ridges travel much slower than the direct signal from the primary source and scattered waves by seamounts arrive after the direct signal as well, the interaction between wave fronts generated by primary and secondary sources leads to difficulties in prediction of arrival time for the tsunami with the largest amplitude.

The importance of seamounts and islands in tsunami trapping and scattering was recognized early in tsunami research by Van Dorn (1970) when he analyzed sea level change caused by the 1957 tsunami recorded at Wake Island. The tsunami of 1964 recorded at Macquarie Island showed a maximum energy at 6 min period which Longuet-Higgins (1967) explained as a trapped long wave by the local bathymetry. A number of theoretical investigations of isolated island/seamount, ridge response to the incoming tsunami signal (see, Murty 1977, Mei, 1989 and Mofjeld et al., 2000 for summary) lead to conclusion that trapped motion can significantly modify the sea level and the currents in the island/seamount proximity. Spectra examinations of the sea level oscillations recorded during tsunami events (Loomis, 1966; Van Dorn, 1984; Rabinovich, 1997, Munger and Cheung, 2008, Horrillo et al., 2008) reveal standing waves and strong resonance amplification related to the local bathymetry and to the frequency window of the arriving tsunami waves.

To investigate tsunami wave amplification and travel time we propose to use energy flux. The source of the tsunami energy is the bottom displacement which defines the total potential energy. This energy constitutes only a small portion of the total seismic energy (Kajiura, 1981; VanDorn, 1984), for example the energy released by the 2004 Indian Ocean earthquake was estimated at 1.1×10^5 TJ (Terra joules) while the potential energy of tsunami was only (Kowalik et al., 2005a) 5.39×10^3 TJ. How the tsunami energy is delivered from the source to subdomains of the global ocean can be investigated through the energy flux pathways. Energy fluxes through major passages between oceans determine the leakage of tsunami energy from the source to the adjacent oceans (Munk, 1963). Along with such integral estimates the energy flux can be used locally to estimate inflow and outflow of the energy at the given geographical location.

We have tested this tool to reveal various aspects of tsunami physics (Kowalik et al., 2005a, b; 2007a, b; 2008). Energy flux, in contrast to the noisy tsunami sea level, reveals uniform behavior in time and space. In addition, it contains information about directionality of the signal which is important for identification of prominent bathymetric features as potential sources of tsunami wave refocusing. We will demonstrate application of the energy flux to generate charts of arrival time of the initial wave and the wave carrying the maximum energy.

Numerical models may serve, not only to produce the extent of coastal inundation and travel time charts to various locations on the coastlines, but also to assess sudden changes caused by higher energy pulses in the late arriving tsunami waves, so that proper decisions can be made on evacuation of people in real tsunami events, as well as for long term planning of the coastal zone development.

Global Tsunami Model and energy balance equation

We will describe and analyze results obtained on the energy flux through the global tsunami model (GTM) constructed and tested by Kowalik et al. (2005b, 2007a, b, 2008). The model includes a high order of approximation for the spatial derivatives (Imamura, 1996; Lynett et al., 2002; Mader, 2004). The boundary condition at the shore line is controlled by the total depth and can be set either to run-up or to the zero normal velocity. The model has been calibrated and tested through comparison to analytical solutions and to laboratory experiments as well.

After extensive testing and comparison, this model, with spatial resolution of 1 arc-minute, was applied to the tsunami of 26 December 2004 in the World Ocean from 80°S to 69°N. Because the computational domain included approximately 200 million grid points, a parallel version of the code was developed and run on a supercomputer. The finer spatial resolution of one arc-minute applied to the World Ocean (Kowalik et al. 2005a, b, 2007a,b) produces very small numerical dispersion even when tsunami waves travel over large distances. GTM due to its high spatial resolution sets the possibility of bringing a wider scope of physical processes into tsunami warning and prediction services.

Results of the GTM comparison against Indian Ocean Tsunami (IOT) recorded information showed quite surprising outcome, namely: a) travel time computation based on Fermat's principle may lead to errors in predicting tsunami arrival, b) passing through the narrows between continents a tsunami signal may reorganize from noisy into coherent wave pattern, and c) Coriolis force can play an important role in the global tsunami propagation.

Application of GTM to numerical simulation of the Kuril Islands tsunami (KIT) of November 2006 (Kowalik et al., 2008) highlighted the behavior of the transoceanic tsunami and the special conditions which cause tsunami enhancement at Crescent City. This investigation demonstrated that the tsunami delay and amplification at Crescent City were caused by both the redirection of tsunami energy over long distances of propagation and by amplification due to the local coastal morphology.

A conclusion from the global modeling applied to Indian and Pacific Oceans is that tsunami waves traveling over global oceans are strongly modified by bathymetry through scattering, refraction and trapping. Enhancement of tsunami amplitude is observed over major oceanic ridges which act as waveguides for tsunami waves, transferring the tsunami energy from thousands kilometers apart without noticeable dissipation. Large seamounts scatter tsunami energy refocusing the tsunami signal more efficiently toward a particular location.

Proposed tools for location of the secondary sources and travel times are based on the energy flux for the non-linear shallow water equations. Equations of motion along E-W and N-S directions (Kowalik and Murty, 1993),

$$\rho \left(\frac{\partial u}{\partial t} + u \frac{\partial u}{\partial x} + v \frac{\partial u}{\partial y} \right) = -g\rho \frac{\partial \zeta}{\partial x} - \tau_x^b/D \quad (1)$$

$$\rho \left(\frac{\partial v}{\partial t} + u \frac{\partial v}{\partial x} + v \frac{\partial v}{\partial y} \right) = -g\rho \frac{\partial \zeta}{\partial y} - \tau_y^b/D \quad (2)$$

and equation of continuity,

$$\frac{\partial}{\partial x} uD + \frac{\partial}{\partial y} vD + \frac{\partial \zeta}{\partial t} = 0 \quad (3)$$

are used to construct the energy conservation equation. In the above set of equations, u and v are horizontal components of the velocity vector, directed along E-W and N-S respectively, ζ is the sea level variation around mean-sea level, τ_x^b and τ_y^b are the components of the bottom stress vector, expressed as $\tau_x^b = ru\sqrt{u^2 + v^2}$, $\tau_y^b = rv\sqrt{u^2 + v^2}$, r is the bottom friction coefficient equal to 0.003, ρ is the density of water, and g is the gravity acceleration. The total depth is $D = H + \zeta$. Here H is the depth measured from the mean-sea level (MSL). In order to derive energy balance equation let us multiply eq.(1) by Du , eq.(2) by Dv , and eq.(3) by $\rho g \zeta$. Adding the resulting equation on either side, we arrive at

$$\begin{aligned} \frac{1}{2} \frac{\partial}{\partial t} [\rho D(u^2 + v^2) + \rho g \zeta^2] + \frac{\partial}{\partial x} \{ \rho u D [(u^2 + v^2)/2 + g \zeta] \} + \frac{\partial}{\partial y} \{ \rho v D [(u^2 + v^2)/2 + g \zeta] \} \\ = -\tau_x^b u - \tau_y^b v \end{aligned} \quad (4)$$

The various terms in the above equation can be defined as follows:

1. $e_k = \rho D(u^2 + v^2)/2$ denotes the surface density of the kinetic energy; it is defined by the velocity and the total depth.
2. $e_p = \rho g \zeta^2/2$ denotes surface density of the potential energy; it is defined by the sea level oscillations around MSL.
3. The second and the third terms in eq.(4) represent the components of an energy flux vector. This vector characterizes the flux of energy through a unit width surface extended from the ocean surface to the bottom. The components of the vector along latitude and longitude are

$$\mathbf{E}_h = \{ \rho u D [(u^2 + v^2)/2 + g \zeta], \rho v D [(u^2 + v^2)/2 + g \zeta] \} \quad (5)$$

4. The tsunami energy dissipation takes place through the bottom stress: $-\tau_x^b u; -\tau_y^b v$.

The full definition of the energy flux vector (eq.5) includes two terms related to potential and kinetic energy. The flux of the kinetic energy $(u^2 + v^2)/2$ in tidal computations and measurements is very small as compared to the flux of the potential energy (Henry and Foreman, 2001). Calculations in the Indian and Pacific Oceans show that the above conclusion is valid for tsunamis as well.

The first order approximation (possibly not valid in the very shallow water)

$$\mathbf{E}_{h1} = \{E_{hx}, E_{hy}\} = \{\rho g H u \zeta, \rho g H v \zeta\} \quad (5a)$$

will serve to describe the tsunami energy flux from the source to various locations.

To demonstrate the concept let's consider the progressive wave along the x-direction (Kowalik and Murty, 1993) for the sea level

$$\zeta = \zeta_a \cos(\omega t - \kappa x) \quad (6)$$

and for the velocity

$$u = \zeta_a \sqrt{\frac{g}{H}} \cos(\omega t - \kappa x) \quad (7)$$

Introducing above expressions into eq. (5a) for the energy flux and neglecting the kinetic energy term, the energy flux reads (Nekrasov, 1992)

$$E_{h1} = \frac{1}{2} \rho g \sqrt{gH} \zeta_a^2 [1 + \cos 2(\omega t - \kappa x)] \quad (7a)$$

The energy flux of the progressive wave is always positive and it changes from zero to the maximum value $\rho g \sqrt{gH} \zeta_a^2$. Its period of propagation is 2 times shorter than that of the sea level or velocity. It is aligned with the direction of propagation, but not with the direction of the velocity which can be positive and negative. Thus plotting the velocity would not yield the same pattern of directions as the energy flux will show, since velocity (eq.7) changes from positive to negative values.

The above formula for the energy flux can be also used to track the maximum energy flux. To achieve this we assume that u is normal to the wave front and when $\omega t - \kappa x = 0$ it follows from eq.(7a) that the energy flux is at maximum. For such simplified case the energy flux is expressed as

$$E_{h2} = \rho g \sqrt{gH} \zeta_a^2 \quad (7b)$$

This formula estimates the energy flux by the sea level only. Hence, along with numerical solutions which require both sea level and velocity for the full calculation using eq.(5a) we can apply observational sea level from buoys or coastal gauges (Koshimura et al., 2008) to calculate energy flux by eq.(7b). Unfortunately eq.(7b) estimates the energy flux maximum only, it does not defines the components of the energy flux vectors as eq.(5a) does, therefore it has no directional properties which are important for the identification of the tsunami energy sources.

Simple experiment – continuous source of tsunami waves

Consider a domain in proximity of the Crescent City (CC) as depicted in Fig. 1. From the western open boundary a continuous wave train of 20 min period and 10 cm amplitude is forced into the domain. At the northern and southern open boundaries the radiating conditions are set. The energy balance equation will be considered inside the box depicted by dashed lines.

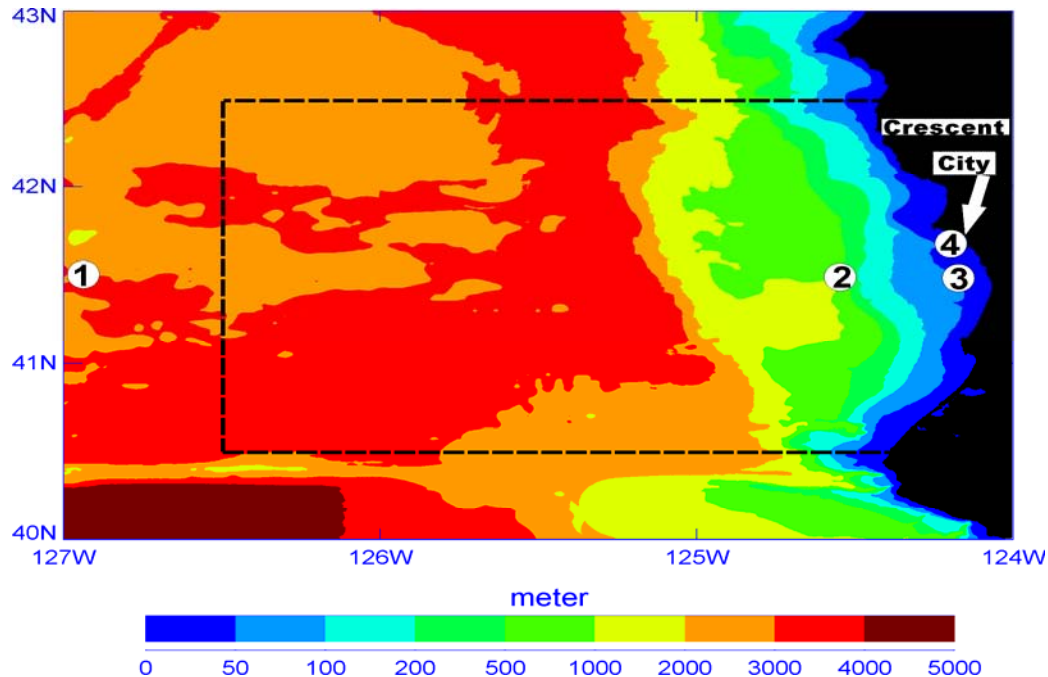


Figure 1. Bathymetry in proximity to Crescent City. Dashed lines denote box for considering energy fluxes. Points 1-4 indicate locations of numerical gauges where sea level and velocity are recorded.

The full stationary state inside the domain has been reached after about 20 periods of incoming wave, although the velocity and sea level are close to the stationary state after approximately 3 periods (cf. Fig.2). The time-history of velocity (east-west component) and the sea level is plotted in Fig. 2. Point 1, located in proximity of the open boundary (depth=2970m), has maximum particle velocity of 0.84cm/s and sea level amplitude of 9.7cm. Waves are strongly amplified in the nearshore region (in point 4 the depth is 0.7m). From point 1 to point 4 the velocity is amplified approximately 155 times while the sea level only 12 times.

The conservation of energy (eq.4) states that in every grid point the change in time of the total energy (i.e. sum of kinetic and potential energy) should be balanced by the energy fluxes (through the walls of the elementary volume $D\delta x\delta y$) and dissipation. If the sea level and velocity change is stationary in time (i.e. repeats itself over wave period) the integration over the wave period should lead to the conclusion that the total energy does not change from one period to the next, and therefore the energy balance will require that the fluxes of energy in/out of the domain should be balanced by the dissipation.

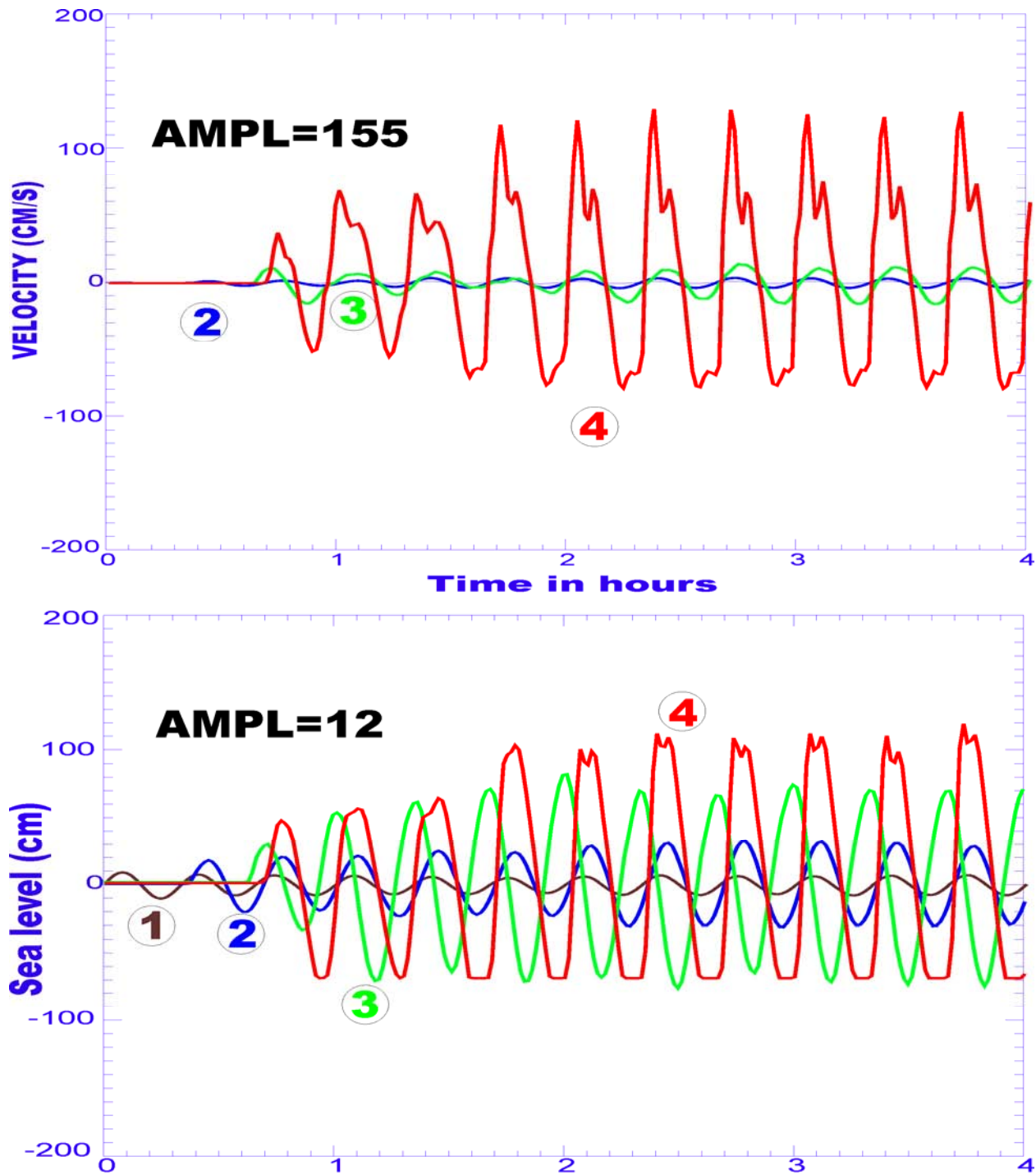


Figure 2. East-west velocity and sea level as a function of time. Recording points are depicted in Fig.1. Amplification coefficient (maximum value at P.4 divided by value at P.1) for velocity (155) is much larger than the amplification for the sea level (12).

The energy inside the domain after 20 periods is quite steady. The double precision calculation shows that the average over 20 min period for the total potential energy (EP) is $EP=4.67579 \times 10^{19}$ watts, while for the kinetic energy (EK) is $EK=4.55895 \times 10^{19}$ watts. Thus the potential and kinetic energy is approximately equal (equi-partitioned), but a very small discrepancy points towards slight dominance of EP.

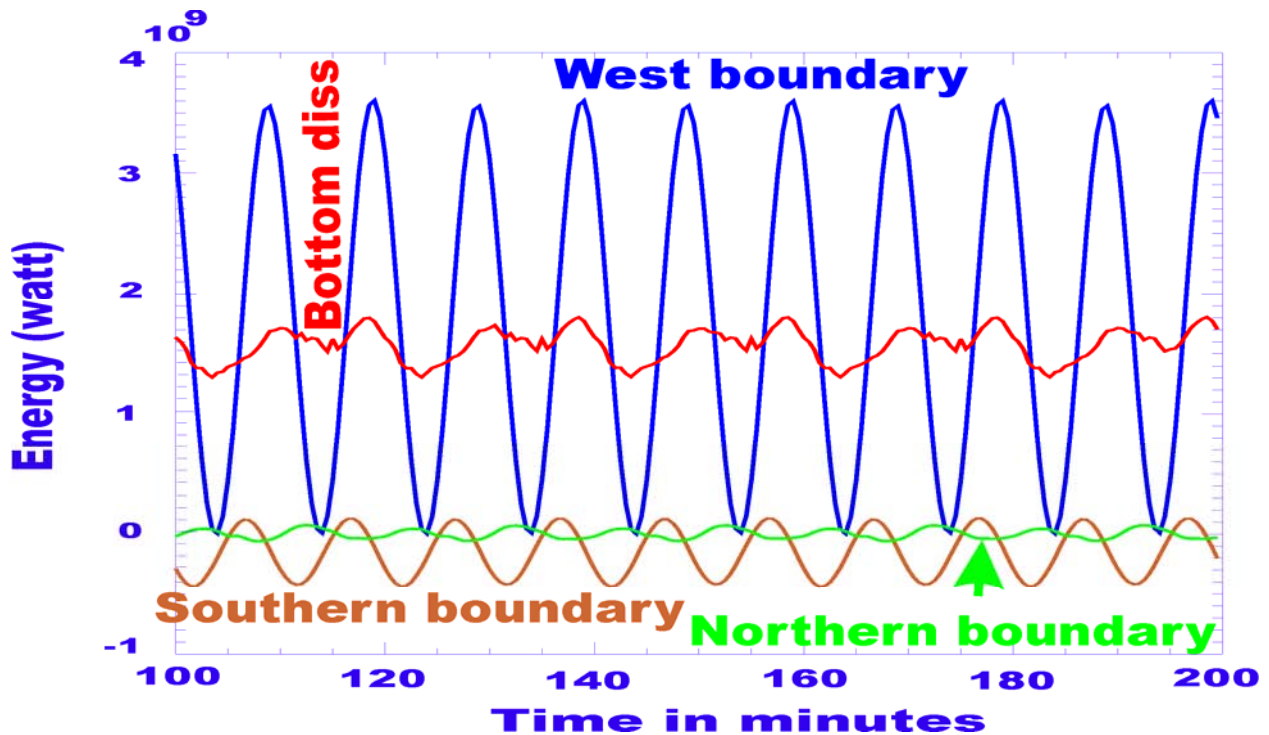


Figure 3. Energy balance for the 20 minute period incident wave in the control box surrounding Crescent City shelf. Energy influx through the western boundary is not completely balanced by the outflowing energy from the northern and southern boundaries and the energy dissipated by the bottom friction.

To investigate the energy fluxes through the open boundaries and the dissipation due to the bottom friction, the major constituents of the energy balance are plotted for 5 periods (between period 25 and 30) in Fig. 3. The inflowing potential energy through the western face of the box, and the outflowing energy through the northern and southern boundaries are periodical in time with the period of 10 min (since amplitude is squared, the period for energy is two times shorter). The bottom dissipation term has the same periodicity but it has unequal amplitudes during each half of the 20 min period wave. The run-up and rundown shown in Fig.2 is the cause of this inequality. The average energy over period (after computed 20 periods) is approximately constant. The inflowing energy (EI) is equal to 1.87162×10^9 watts and the outflowing energy is -1.56555×10^8 watts. The energy dissipated due to the bottom friction is equal to -1.61626×10^9 watts and plays the main role in the balancing inflowing energy. The outflowing and dissipated energy (EO) result in -1.77282×10^9 watts, thus not completely

balancing the inflowing energy. The difference between these two numbers is small; nonetheless it introduces an important question, namely what is happening to the undissipated inflowing energy since the total energy inside the control box is constant, but due to undissipated energy ought to grow in time. This problem is discussed in detail in the Appendix.

Energy flux application for tsunami physics

To demonstrate that the energy flux will be a valuable addition to the science of tsunami hazards we focus on the results obtained by application of the global tsunami model (GTM). A GTM was applied to investigate the Indian Ocean Tsunami (IOT) of December 26, 2004 and Kuril Islands Tsunami (KIT) of November 15, 2006 (Kowalik et al., 2005a,b, 2007a,b, 2008; Horrillo et al., 2008). The major result from these computations was an enhanced understanding of the tsunami wave trains origin arriving at the distant locations sometimes a few hours after an initial (forerunner) wave. Tsunami waves traveling over the global ocean are strongly modified by bathymetry through scattering, refraction and trapping. Enhancement of tsunami amplitude was observed over major oceanic ridges which act as wave guides for tsunami waves, transferring the tsunami energy from thousands kilometers apart without noticeable dissipation (Koshimura et al., 2001; Kowalik et al., 2005a, 2007b, 2008; Titov et al., 2005; Lay et al., 2005; Hirata et al., 2005).

The GTM for the IOT demonstrated how tsunami propagated over the entire World Ocean. In the Indian Ocean the tsunami properties were related to the source function, i.e., to the magnitude and direction of the sea bottom displacement. The leakage of energy into the Atlantic Ocean (between Africa and Antarctic) showed a unidirectional pattern since the energy was pumped into this domain through the directional properties of the source function. Nonetheless both observations and models showed strong tsunami in Pacific as well. The main questions were: How the energy was redirected into Pacific? What are mechanisms for redirection and how much energy entered the Southern Pacific Ocean?

To answer above questions, an energy flux is considered (Kowalik et al., 2005b, 2007a) through the three cross-sections located between Antarctica and the major continents. The cross-section (blue color in Fig. 4) along the longitude 20°E from Antarctica to South Africa (AS) shows the time variation of the energy flux between Indian and Atlantic Oceans (eastward is the positive direction). This flux remains negative for the entire period of 50 h, thus confirming that the inflow is directed into the Atlantic Ocean. On the other hand, the energy flow through a cross-section along 140°E (green color) extended from Antarctic to Australia (AA) is at all times positive (from the Indian to Pacific Oceans). The flux through the cross-section located between South America and Antarctica at 70W (red color), reveals a small inflow from the Atlantic into the Pacific.

Fig. 4 clearly demonstrates that the magnitude and the time variability of energy fluxes through cross-sections AA and AS are quite different in character. The flux passing AS has a large value and the maximum energy inflow to the Atlantic is located close to the initial wave front, even though the first arriving signal is not related to the maximum energy.

The energy flow into the Atlantic is a result of the source orientation. The energy flow through AA demonstrates that tsunami arrives to this cross-section about 10 h from the onset of the earthquake; it initially has small amplitude which slowly increases in time from 18 to 21 h to achieve a few maxima.

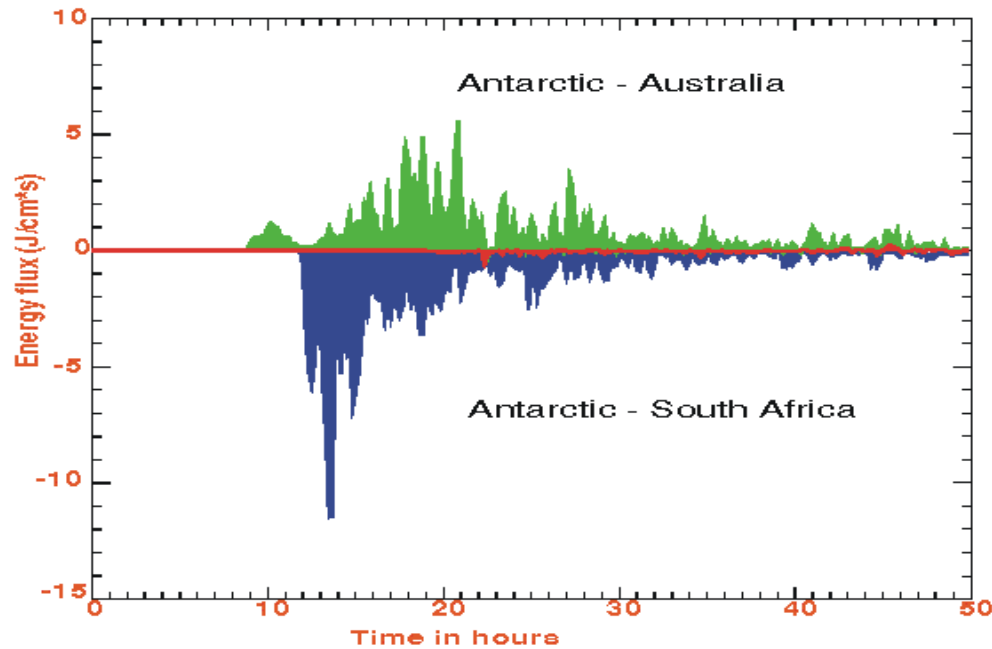


Figure 4. Energy flux through the cross-sections located between Antarctic and major continents. Along 20E from Antarctic to South Africa (AS), blue color, along 140E, from Antarctic to Australia (AA), green color, along 70W from South America to Antarctic, red color (after Kowalik et al., 2005b).

Analysis made by Kowalik et al., (2005b, 2007b) demonstrated that the maxima from 18 to 21 h in Fig. 4 were related to the energy flux arriving by the various routes from the Indian Ocean. The arrival time of these signals depends on the depth and on the traveled distance. Signals which travel from the generation area to the section AA through the deep ocean travel faster, in about 10 h, but transfer less energy. The large inflow of energy shown in Fig. 4, is related to the reflected signals off the Seychelles, Maldives and Africa, and to a slow wave which traveled along ridges that was originated through reflections in the Bay of Bengal. To compare the total energy flux entering Pacific and Atlantic Oceans over the first 50 h of process, the energy fluxes given in Fig. 4 have been integrated in time. The total energy leakage into the Pacific Ocean is approximately 75% of the total leakage to the Atlantic Ocean. This large value is quite remarkable considering that the source directs energy into the Atlantic Ocean and the energy is re-routed into the Pacific by reflections. As pointed out by Murty et al., (2006), the Indian Ocean resembles an elliptical shape which has a tendency to multiple reflections and focusing. Fig. 4 is closely related to the time-history of the tsunami energy in the Indian Ocean. Van Dorn (1984) and Candella et al.(2008) deduced from the coastal observations that the tsunami energy

has an exponential decay in time. The energy leakage to the Atlantic and Pacific (Fig. 4) shows a similar pattern in time. After an initial build up, the energy started to decay in time but the decay pattern is dominated by strong energy pulses, due to multiple reflections and energy trapping along the ridges, islands and seamounts.

The energy time-history in the oceans adjacent to the Indian Ocean will be even more complicated due to the fact that the tsunami temporal and spatial variability is restructured while tsunami travels through the narrow passages between oceans (cf. Kowalik et al., 2007b, Fig.10.11, p. 109). The tsunami signals in the Northern Atlantic and Southern Pacific have been strongly reorganized into coherent wave trains after passing through the narrows between Africa and South America, and Australia and Antarctica. To the lesser extent the same process was taking place for the tsunami entering into the Atlantic (between Africa and Antarctica) and for the waves entering the Pacific from the Atlantic (between South America and Antarctica).

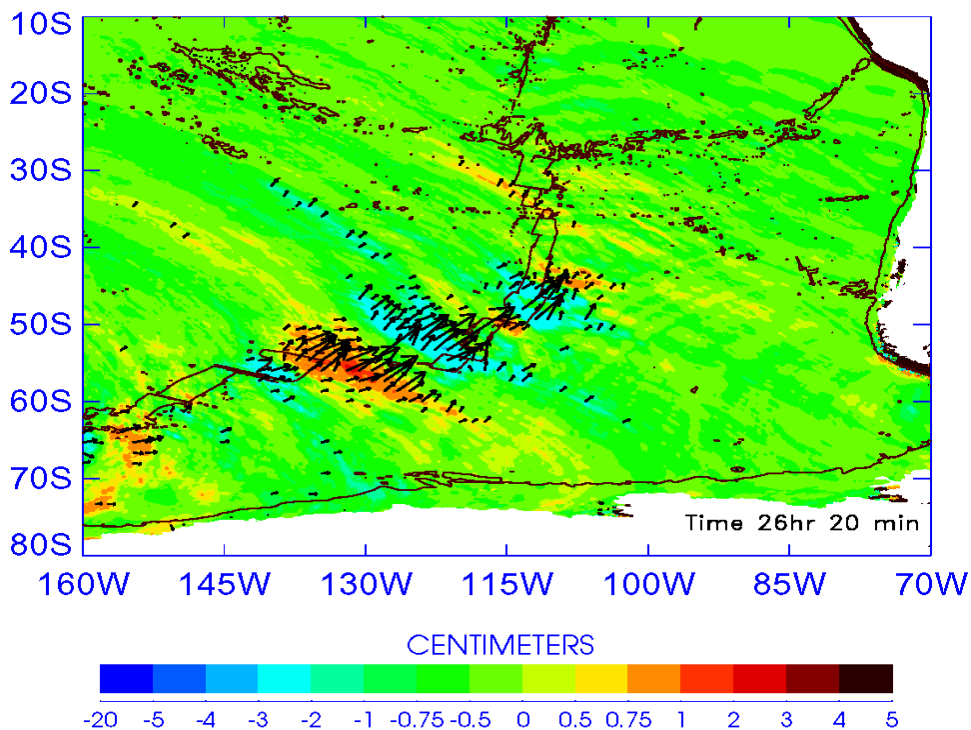


Figure 5. Energy flux vectors over the South Pacific Ridge at time 26h 20min from IOT onset. The colors denote the sea level. The dark-brown lines denote the ridge depth - 3000m depth contour.

The energy flux vectors in Fig. 5 demonstrate that the slower signal travels along oceanic ridges and transfers more energy. In this figure, the energy flux vectors are shown in the south-western part of the Pacific Ocean. The larger tsunami amplitudes are located above the oceanic ridge and the energy flux vector is directed along the ridge (notice that vector does not change direction over positive or negative sea level). This small group of higher amplitude waves does not belong to the first tsunami signal to arrive in this region. Its average wavelength is about 1350 km, as the depth of the ridge is close to 3 km, the wave period is about 2 h. The tsunami enhancement is partly related to the presence of the South Pacific Ridge but this strong and coherent group of

waves was generated out of the chaotic signal while passing through the strait between Australia and Antarctic (Kowalik et al., 2005a, b; 2007b).

In the wake of Kuril Islands Tsunami (KIT) of November 15, 2006, the sea level at Crescent City (CC) initially changed up to 20 cm and 2-3 hours later the highest wave of about 90 cm amplitude was recorded. Numerical experiments using GTM (Kowalik et al., 2008) identified the bathymetric features which scatter the tsunami signal towards CC via the Mendocino Escarpment (Fig. 6). This escarpment seems to be efficient in delivering enhanced tsunami energy if the approaching tsunami signal travels from the west along the escarpment.

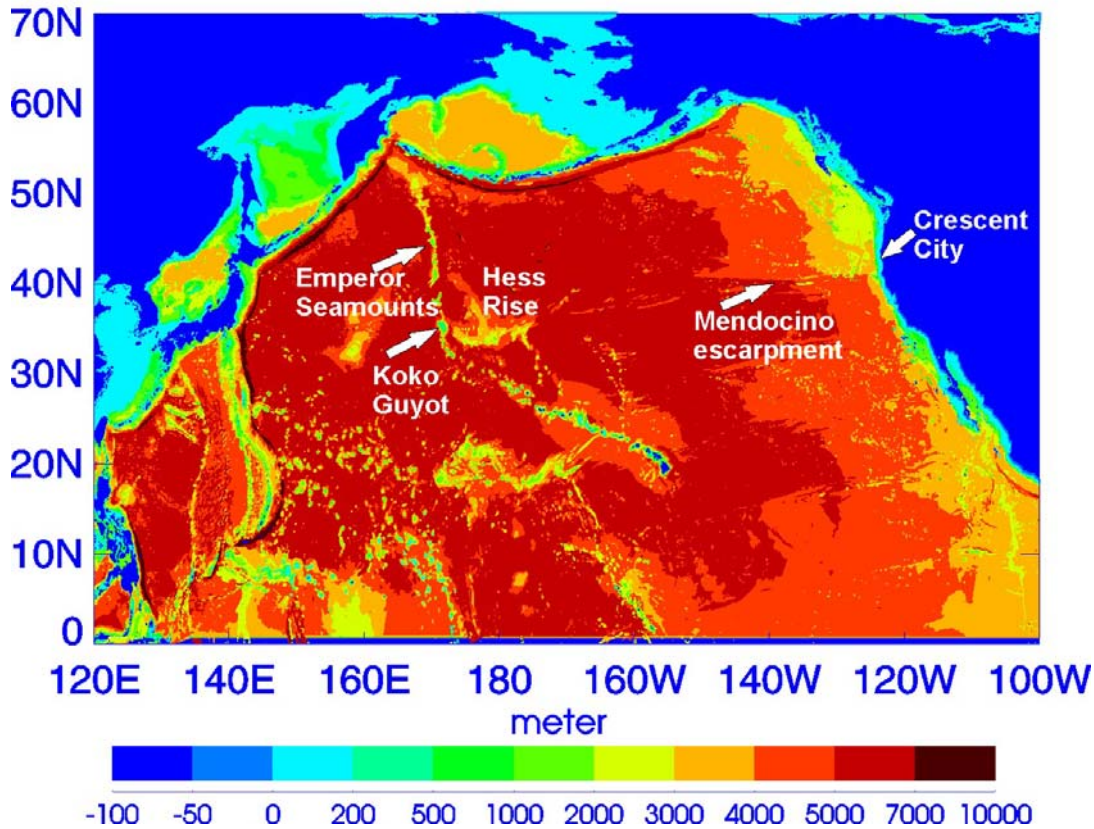


Figure 6. Bathymetry based on the one-minute grid. Shown are main bathymetric features important for the tsunami arriving at Crescent City.

To investigate the pattern of the energy trapped over Mendocino Escarpment the energy flux was used. A simple experiment was performed to demonstrate the wave trapping by this bathymetric feature. Three waves of 16 minutes period each and 10 cm amplitude were sent towards the west coast of North America from the open boundary located at 150W (Fig. 7, left panel). In Fig. 7 (right panel) the wave pattern 160 minutes later is shown. The energy flux vectors in these figures demonstrate the strong local amplification of energy during wave propagation towards CC. The wave amplitude shows a corresponding strong local amplification as well. The wave front curvature focuses the energy flux vectors slightly up north from the Mendocino Escarpment.

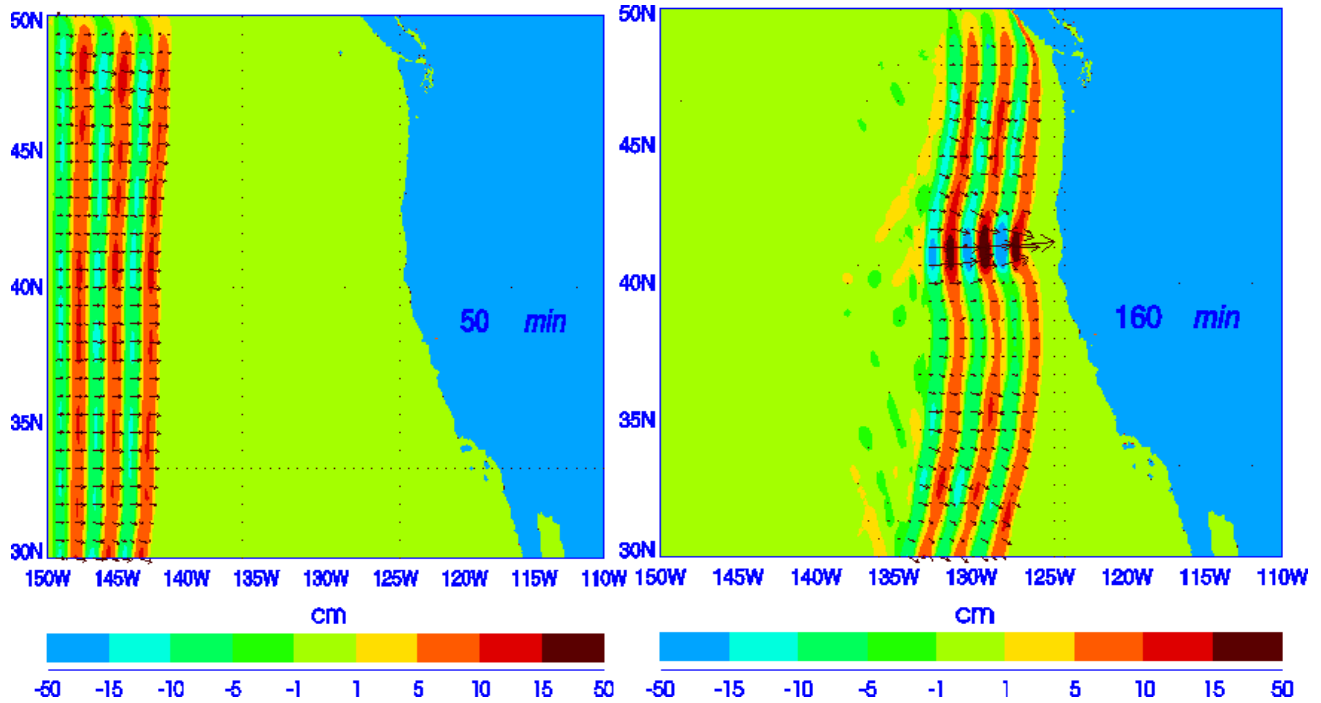


Figure 7. Three waves of 10 cm amplitude and 16 min period travel parallel to the Mendocino Escarpment. Amplitude given by colors. Vectors denote energy flux (after Kowalik et al., 2008a)

The time-history of the energy flux traveling towards CC during the Kuril Islands tsunami of 2004 was analyzed by considering a similar box as in Fig. 1. The box around CC was constructed as follows. The west boundary is located at 129W, the north boundary at 44.5N, the south boundary at 39.5N and the east boundary is on land. The time dependent energy flux was averaged over the length of each boundary.

The results given in Fig. 8 show two distinct pulses of energy crossing the western face of the box towards CC. Within the second pulse, 2 maxima occur separated by 20 minutes time interval. It is interesting to see that there is very little reflected energy coming back across the faces of the box. This must mean that most of the incident energy is dissipated by the near shore bottom friction.

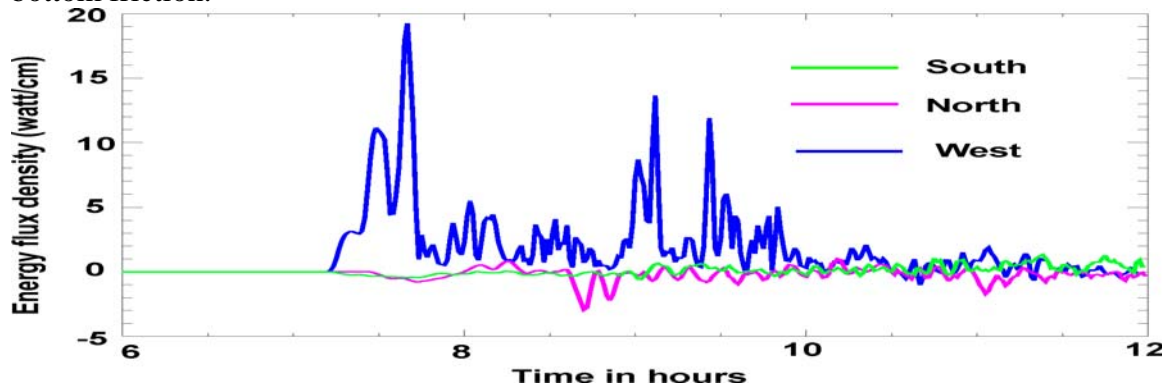


Figure 8. Energy flux through the western (blue), northern (red) and southern (green) walls of a 5 degree box around Crescent City (adapted from Kowalik et al., 2007a).

Energy flux through the faces of the box around CC can be easily applied to pinpoint the source of the second wave packet. First, we simply remove from the bathymetry the Hess Rise by setting it to the depth of 5000 m. Next, the Koko Guyot is removed in the same manner (both located at the southern end of Emperor Chain, see Fig. 6).

In Fig. 9 the energy flux crossing the western wall is plotted; in the upper panel the Hess Rise is removed but the Koko Guyot stays unchanged and in the lower panel the Koko Guyot has been removed while the Hess Rise remains unchanged. For comparison the energy flux across the western face from Fig. 8 is also given.

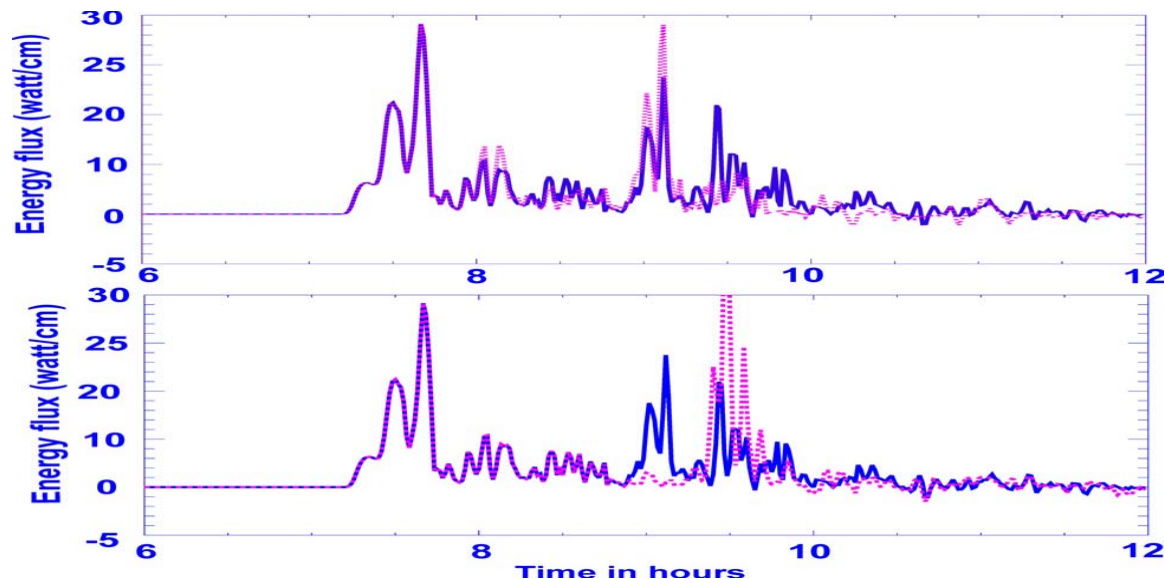


Figure 9. Energy flux through the western wall of a 5-degree box around Crescent City. Blue line: regular bathymetry. Red line: a) upper panel: Hess Rise is removed from bathymetry; b) lower panel: Koko Guyot is removed from bathymetry (adapted from Kowalik et al., 2008a)

The absence of Koko Guyot resulted in a restructuring of the energy flux through the western face of the box in such a way that the first maximum in the second wave group practically disappeared (Fig. 9, lower panel). The second maximum in this later arriving wave group, as the upper panel shows, is related to the Hess Rise. The absence of the Hess Rise leads to energy amplification from the Koko Guyot. As the first group of waves in Fig. 9 does not change in the above experiments we can also conclude that the first group of waves to arrive at CC must travel a route unobstructed by either Koko Guyot or the Hess Rise.

The immense influence of the Koko Guyot on tsunami signal scattering is due to its size and strong contrast between shallow and deep waters. It rises from the depth of 4750 m to within 250 m of the ocean surface (Davies et al., 1972).

Identification secondary sources by tracking energy flux in the Northern Pacific

We have used energy fluxes to elucidate the amplification processes during KIT propagation towards Crescent City. We continue investigation of the same tsunami to work out an approach for identification of the sources of the high amplitude secondary signals and to illustrate the

time delay between initial tsunami wave and secondary signals. The bathymetric features which are important for tsunami arriving at Crescent City have been described in Fig. 6.

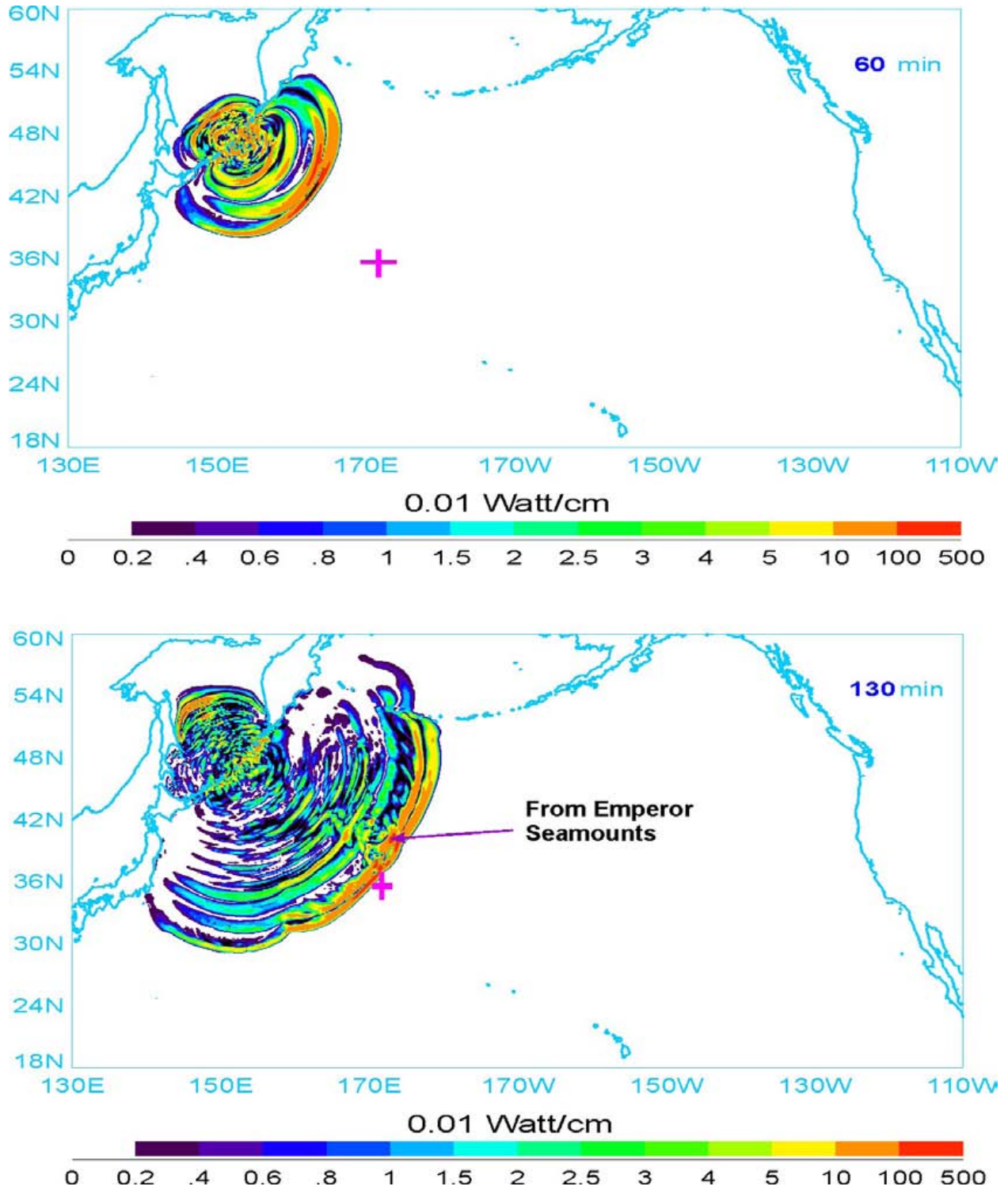


Figure 10. Energy flux contours, 60 min (upper panel) and 130 min (lower panel) after tsunami onset. Red plus marker points to location of Koko Guyot seamount.

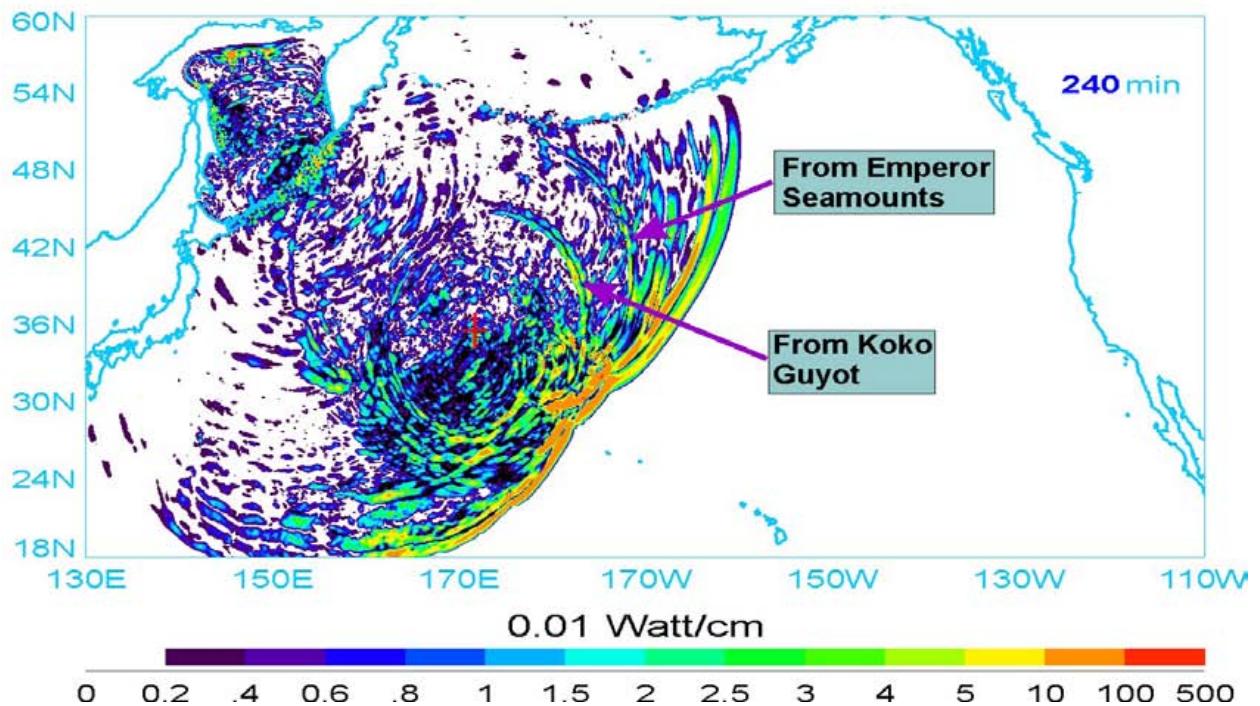
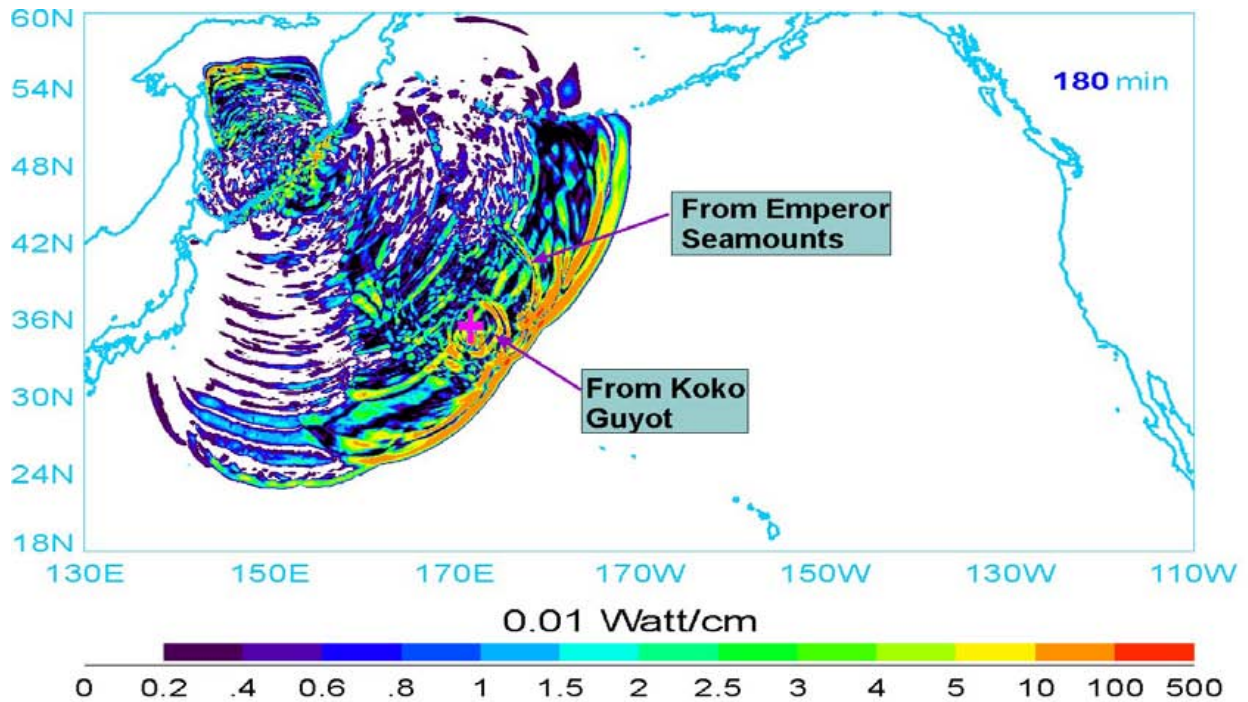


Figure 11. Energy flux contours, 180 min (upper panel) and 240 min (lower panel) after the tsunami onset. Two signals of higher energy have been identified as scattered from the Emperor Seamounts and the Koko Guyot. Note that only the second stronger front is centered on the Koko Guyot. Red plus marker points to location of the Koko Guyot seamount.

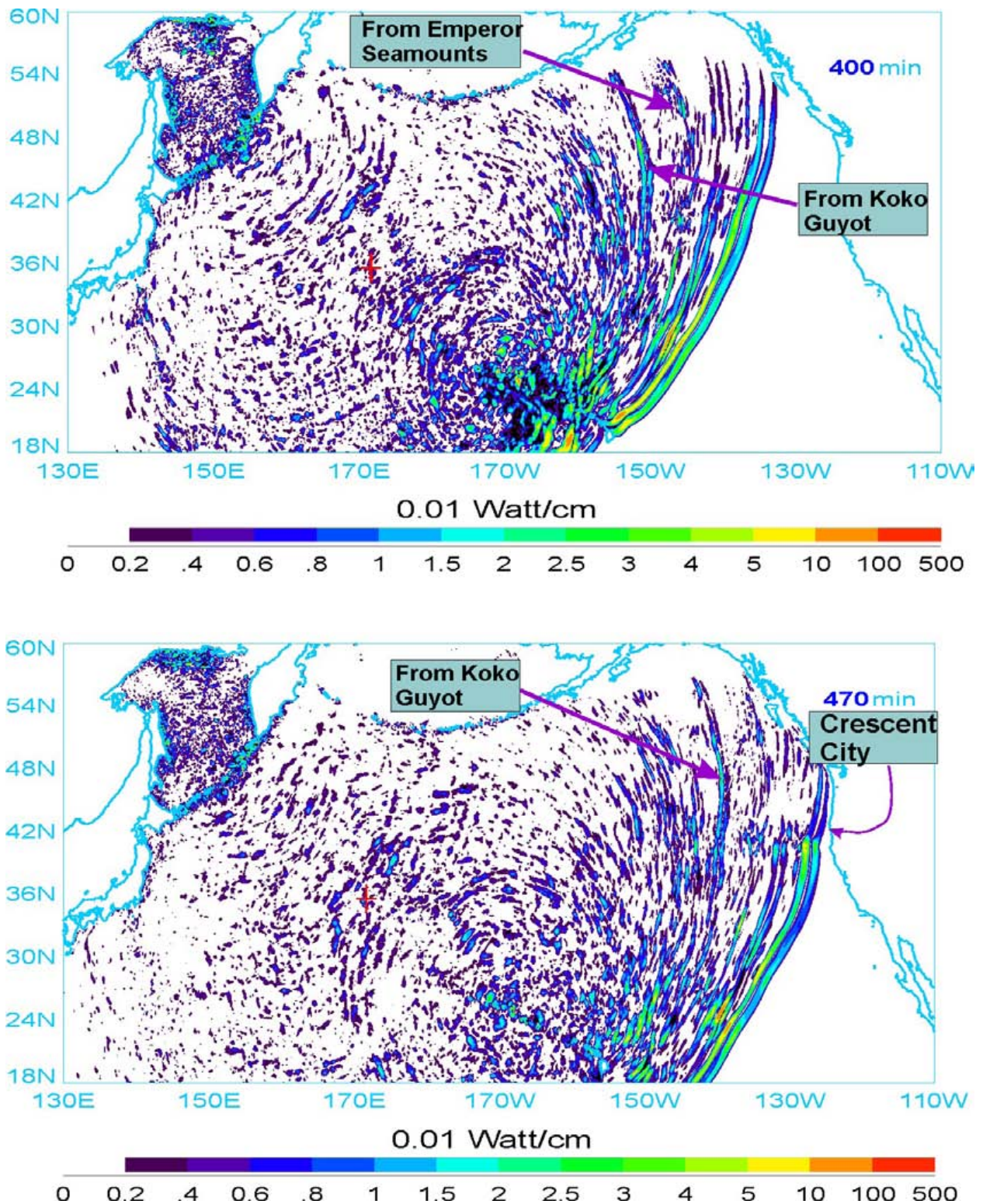


Figure 12. Energy flux contours, 400 min (upper panel) and 470 min (lower panel) after the tsunami onset. Note: a) The signals from Emperor Seamounts have dissipated, b) The first wave arriving to the proximity of Crescent City shows enhancement by the Mendocino Escarpment. Red plus marker points to location of the Koko Guyot seamount.

To further identify important stages in the KIT development the time history of energy flux contours is given in Figs. 10-12. The contours are given by $\mathbf{E}_c = \sqrt{E_{hx}^2 + E_{hy}^2}$. Here the energy flux components are defined by eq.(5a). Sixty minutes after the tsunami onset (Fig.10, upper panel) the tsunami front in the Northern Pacific shows two closely spaced maxima. Notice that these maxima are related to the initial wave's positive and negative amplitudes. The two maxima can be easily tracked in all figures up to the arrival at Crescent City (Fig. 12, lower panel).

Important bathymetric feature in tsunami scattering is Emperor Seamount chain, its influence is depicted 130 min after the tsunami onset by distortion of the primary and secondary wave fronts.

To identify the Koko Guyot as an important bathymetric feature, we plot in Fig. 11, upper panel, the energy flux contours immediately following passage of the main energy lobe past Koko. Note that only the second front is centered on the Koko Guyot, the first front has been generated by the Emperor Seamount Chain and it is not centered on Koko Guyot. Further time history given in Fig. 12 shows that the energy maximum due to the Emperor Seamounts has been significantly dissipated and the stronger energy fluxes are associated with the primary wave and the wave scattered from the Koko Guyot. Not only tsunamis on the US shores were influenced by these bathymetric features, as Koshimura et al. (2008) showed the tsunami scattered from the Emperor seamounts strongly influenced the maximum tsunami energy along the Pacific coast of Japan, as well.

Above experiments by using energy flux defined in the explicit way the bathymetric features which scatter tsunami signal towards Crescent City, via the Mendocino Escarpment. Identification of the distant bathymetric features was achievable since the energy flux delineates the energy pathways that couple bathymetric features (Koko Guyot and the Hess Rise) to the Crescent City located thousands of kilometers apart.

Tsunami travel time

Application of energy fluxes for tracking the large amplitude tsunami waves will result in the prediction of arrival time for these waves. Both observations and numerical models show that, during IOT in many locations along the Pacific and Atlantic coasts, the first arriving signal, forerunner had lower amplitude than the main signal, which often was much delayed (Rabinovich et al., 2006; Kowalik et al., 2005a, 2007a,b). Understanding this temporal distribution of tsunami characteristics is important for the application to tsunami warning and prediction procedures and technology. Fig. 4 shows that the signal from the tsunami source directed into Atlantic Ocean arrives practically unobstructed carrying maximum amplitude close to the arrival time of the first wave. The situation is quite different for the tsunami entering into Pacific Ocean. The path through the deep Indian ocean carried miniscule energy and the signal arrives at 9 h from the tsunami onset, while the stronger signal arrived to the cross-section at approximately 16 h. A similar processes occurred while the tsunami signal traveled over the Southern Pacific towards the Americas. The path through the deep ocean to western North America again carried miniscule energy, while the stronger signal traveled a much longer distance via South Pacific ridges (cf. Fig. 5). As tsunami travel time from the source region to the given location is an important parameter in the tsunami prediction and warning we intend to investigate in detail this parameter based on our computation of the IOT. The IOT arrival times

have been determined for many locations (Merrifield et al, 2005; Rabinovich et al., 2006). We performed numerical experiments to delineate the tsunami arrival time in IOT by using GTM at every grid point for a signal of 0.1 cm amplitude. The computed tsunami travel time chart is depicted in Fig. 13. The chart shows that even at such small limiting amplitude the tsunami signal arriving at Alaska and North America did not pass through the Indonesian Straits but rather around Australia and New Zealand.

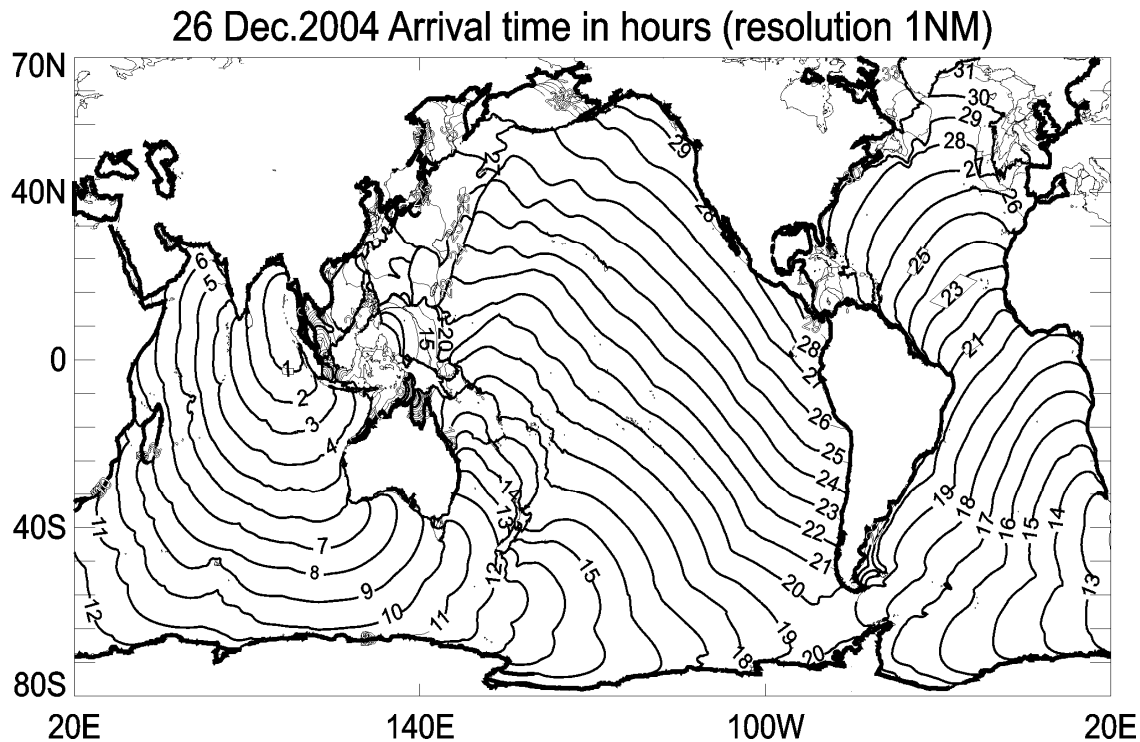


Figure 13. Travel time (in hours) for arrival of the tsunami of 0.1cm amplitude during the IOT of Dec. 2004.

The next numerical experiment computes isolines of arrival time for the tsunami signal of 0.5 cm amplitude (Fig. 14). In the vast regions of the Northern and Central Pacific this figure does not show a consistent arrival time. We may conclude that the main premise used to construct these figures, namely that the first train of tsunami waves is associated with the 0.5 cm amplitude, does not hold true.

We were able to construct isolines of arrival time in the regions of larger amplitudes, i.e. in the Indian Ocean, in the South Pacific (especially along the South Pacific Ridge) and in the South Atlantic. By checking results of computations at the coastal locations we found that a tsunami of 0.5 cm amplitude arrived at every location in the Pacific Ocean. This wave did not arrive at the western North America by refracting around New Zealand; it traveled closer to South America via energy ducts located over South Pacific ridges. This is a much longer travel time compared to the travel time depicted in Fig. 13.

The observations define travel times uniquely when the amplitude of the signal is above the noise level. The mixed signal of meteorological/oceanographic and tsunami origin is difficult to differentiate. Probably the tsunami amplitude of a few centimeters is strong enough to be seen

above the meteorological noise. Therefore, the observed arrival time is usually much longer than the calculated, for example, at Jackson Bay NZ the arrival time was 18 h 18 min, while according to the travel time computed by the first perturbation of 0.1 cm at this location, the arrival time for the first wave was 12 h 30 min.

26 Dec.2004 Arrival time in hours (resolution 1NM)

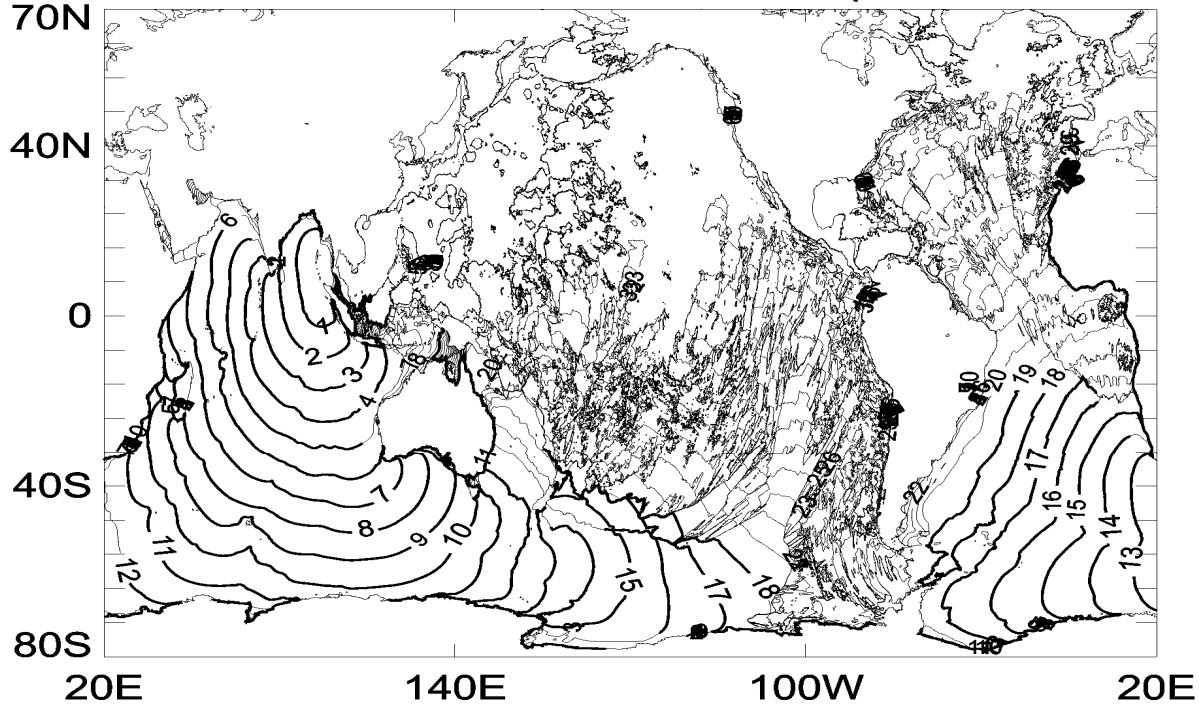


Figure 14. *Travel time (in hours) for arrival of the tsunami of 0.5cm amplitude during the IOT of Dec. 2004.*

Stations located in the Northern Pacific showed the largest differences between the calculated and observed travel time (Kowalik et al., 2005a, 2007a,b). This is caused either by small tsunami signal-to-noise ratio, or by multiple paths between the source and gauge locations. The higher energy tsunami signals arriving at distant locations are usually those which travel slowly over oceanic ridges.

In the Southern Pacific, wave energy ducting marked tsunami propagation over oceanic ridges. Travel times obtained from computations as arrival of the first significant wave show a clear and consistent pattern only in the region of high tsunami amplitudes and in the simply connected domains, such as in the case of the tsunami which traveled from Indonesia, around New Zealand, and into the Pacific Ocean. Described wave behavior indicates that the computations of tsunami travel time based on the ray theory of wave propagation and on Fermat's principle of least time might lead to large errors in predicting travel time for tsunamis large enough to propagate into contiguous oceans. Therefore, to identify the travel times for the large amplitude tsunamis we propose to use the time dependent energy flux contours as shown in Figs. 10-12.

Conclusions and discussions

It is important to recognize that the failure to predict the arrival time of the maximum tsunami in the wake of Kuril Islands Tsunami is due to lack of the proper tools being used by Tsunami Warning Centers. To investigate tsunami wave amplification and time delay we use energy flux. This tool, when tested against IOT of 2004 and KIT of 2006, shows that strong secondary signals are generated by scattering, reflection and refocusing of the primary tsunami wave.

The tsunami scattering by seamounts and trapping along ridges and escarpments needs to be further investigated to understand how the signal is changed during the tsunami/bathymetry interactions. We cannot solely rely on experiments like those done for the Koko Guyot in Figs. 11 and 12. Although the bathymetric features responsible for the tsunami scattering have been identified, we did not arrive at a complete understanding of the generation, scattering and trapping by the Koko Guyot. One of the important results from Figs. 11 and 12 is that the scattering from the Koko Guyot has extended the duration of the Kuril Islands tsunami and scattered signal showed directional modulation which resulted in stronger tsunami in the distant locations. Directional and temporal properties of the tsunami signal in proximity to the bathymetric features depend on the superposition of two waves; a primary wave arriving from the tsunami source and a secondary wave generated by the bathymetry. One can straightforwardly assume that such superposition (cf. Lautenbacher, 1970, Fujima et al., 1995; Liu et al., 1995) generates larger amplitudes at the island's perimeter by refraction process, however there is no straightforward approach to deduce temporal changes in the wave trapped around the island/seamount. The question is how the trapped energy decay in time? Often decay is relatively short in time when caused by the nonlinear frictional dissipation. However, sometimes such waves have been observed to last for a long period of time, pointing towards the existence of trapped and partially leaky modes of oscillations (Yanuma and Tsuji, 1998; Nirupama et al., 2006), interaction between oscillations trapped at the coast and the continental slope (Nekrasov, 1970; Horrillo et al., 2008) and possibly to generation of the dispersive, coastally trapped edge waves (Kurkin and Pelinovsky, 2002).

The search for the resonance periods which are responsible for the tsunami energy trapping is often based on an assumption of stationary oscillations in the primary wave arriving from the source. The short and variable in time tsunami train impinging on a bathymetric feature does not develop the full resonance response (Munk et al., 1956; Horrillo et al., 2008). Examination of tsunami signals (Kowalik et al., 2008) scattered from the bathymetric features also shows stronger energy of shorter wave periods when compared with the primary tsunami signal arriving from a source. As Mofjeld et al., 2000 have noticed these short period waves also contribute to the random appearance of tsunami time series when waves reflected from various bathymetric features interact with each other.

An intermittent behavior of the tsunami train seems to be the crux of all problems related to response calculation of tsunami impinging on seamounts and ocean ridges: shorter and longer tsunami trains result in different enhancement and trapping (Munk et al., 1956; Horrillo et al., 2008). In the above applications to the Indian Ocean Tsunami of 2004 and the Kuril Islands Tsunami of 2006, we have demonstrated that sudden changes caused by higher energy pulses in the intermittent tsunami wave trains can be assessed by energy fluxes. These experiments defined in explicit way the bathymetric features which scatter tsunami signal towards ports, like Crescent City. The identification of the distant bathymetric features was

achievable since the energy flux delineated the energy pathways that coupled bathymetric features (like Koko Guyot) to ports located thousands of kilometers apart.

APPENDIX

Tsunami energy balance and numerical dissipation

As we found in the domain adjacent to the Crescent City the total energy balance which seems to account for all sources and sinks did not balance (Fig. 3). Since the energy inflowing into the domain was not completely dissipated by the frictional forces and at the same time the total energy or sea level did not increase in time, therefore, this fact points towards an numerical dissipation. We shall demonstrate that the additional energy dissipation usually occurs in the short spatial or temporal scales where numerical schemes are unable to resolve wave propagation. Processes of destruction of the tsunami waves due to the short wave dissipation/dispersion are well observed when the wave travels in an upsloping channel (Kowalik, 2003).

To investigate the role of numerical friction, the wave propagation experiment in the 3000km long channel closed at both ends is considered. The shape of the channel is given in Fig. 15.

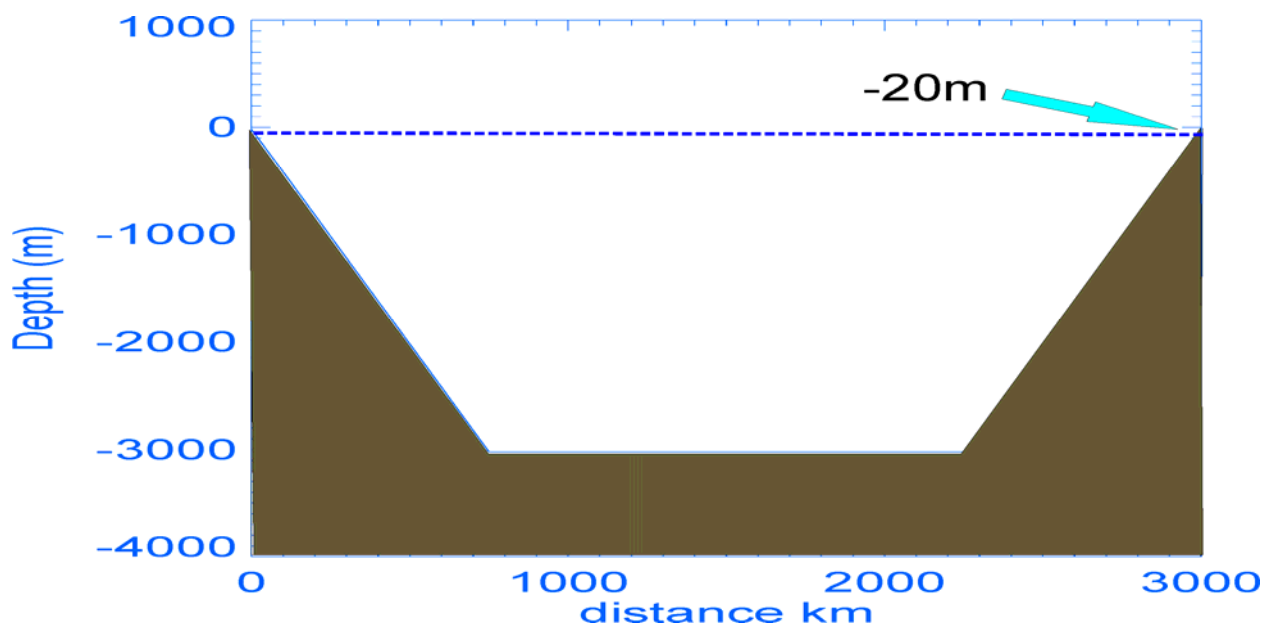


Figure 15. Bathymetry of a channel. Constant depth of 3km at the central part. At the distance of 750km apart from the shores, sea-bottom slopes change linearly to achieve 20m depth at the shores.

The tsunami wave is generated by the bottom displacement in the center of the channel. The high spatial resolution is achieved by the 10m-space step. The time step of 10^{-2} s is used. In the first experiment, a rectangular bottom displacement of 100km length and 2m height generates the sea level change in the center of the channel which propagates both to the left and the right shores as shown in Figure 16.

As the waves propagate towards the shores, even in the deep water, the rectangular signal starts to change by generating short numerical dispersive waves in the front and in the tail of the sea level displacement. Such behavior demonstrates that the numerical scheme with finite resolution is not able to reproduce a square wave without losing energy either through dissipative or dispersive numerical processes.

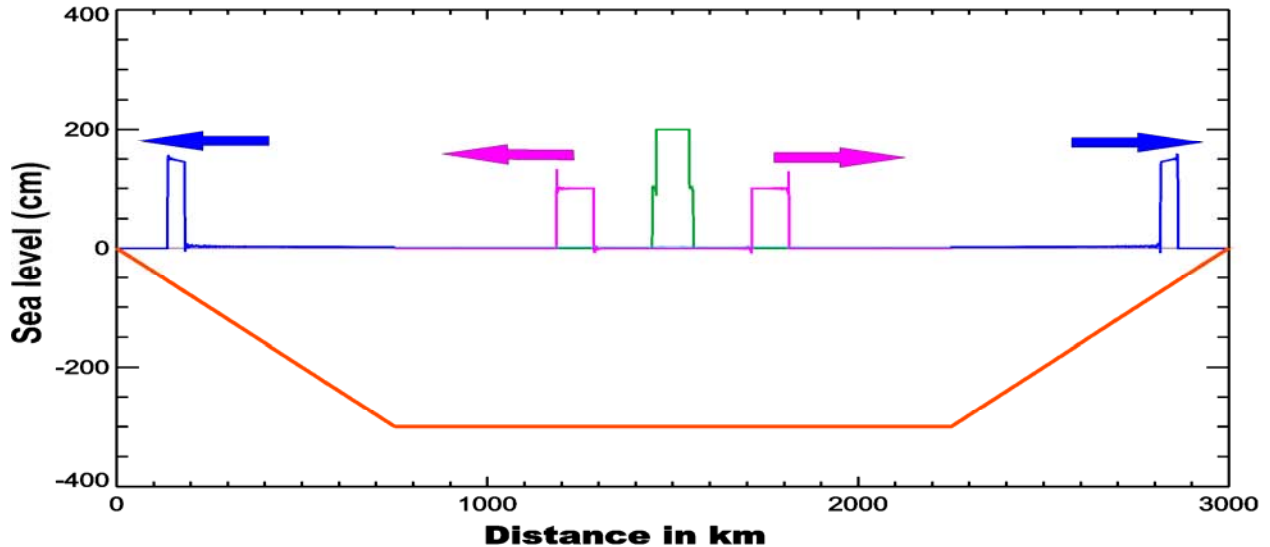


Figure 16. A rectangular bottom displacement of 100 km long generates two waves propagating towards the left and right shores. Notice dispersive waves in the front and tail of the main displacement.

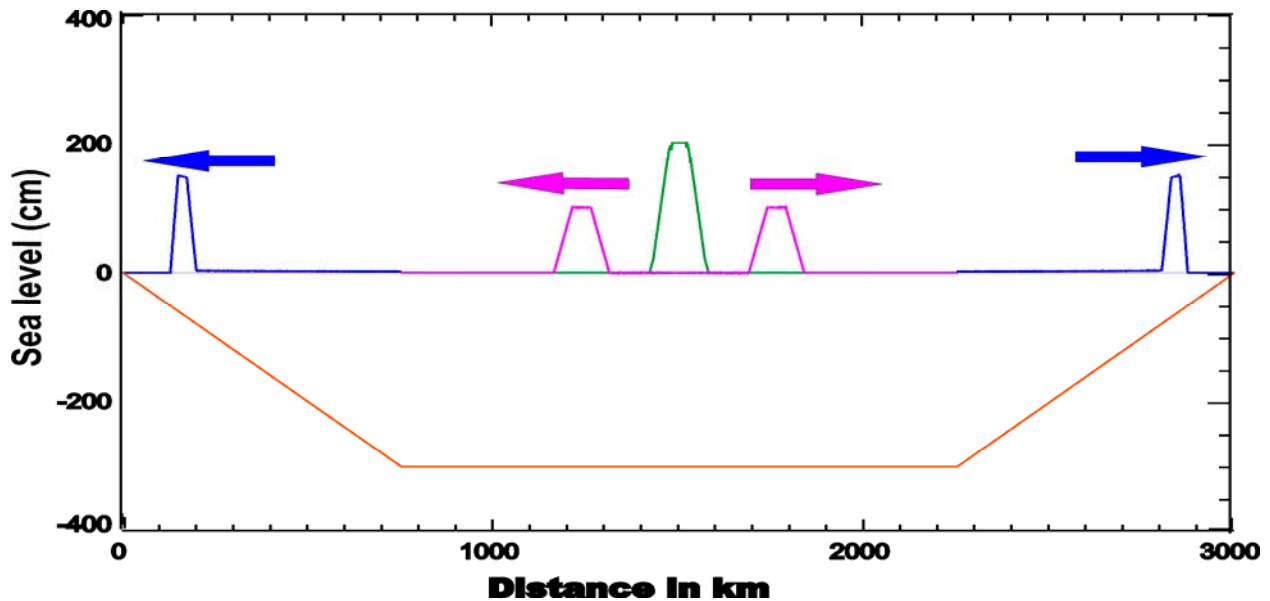


Figure 17. A trapezoidal bottom displacement of 100 km long generates two waves propagating towards the left and right shores. Notice the lack of numerical dispersive waves in the front and tail of the main displacement.

The time-history of a trapezoidal bottom displacement is shown in Fig. 17.

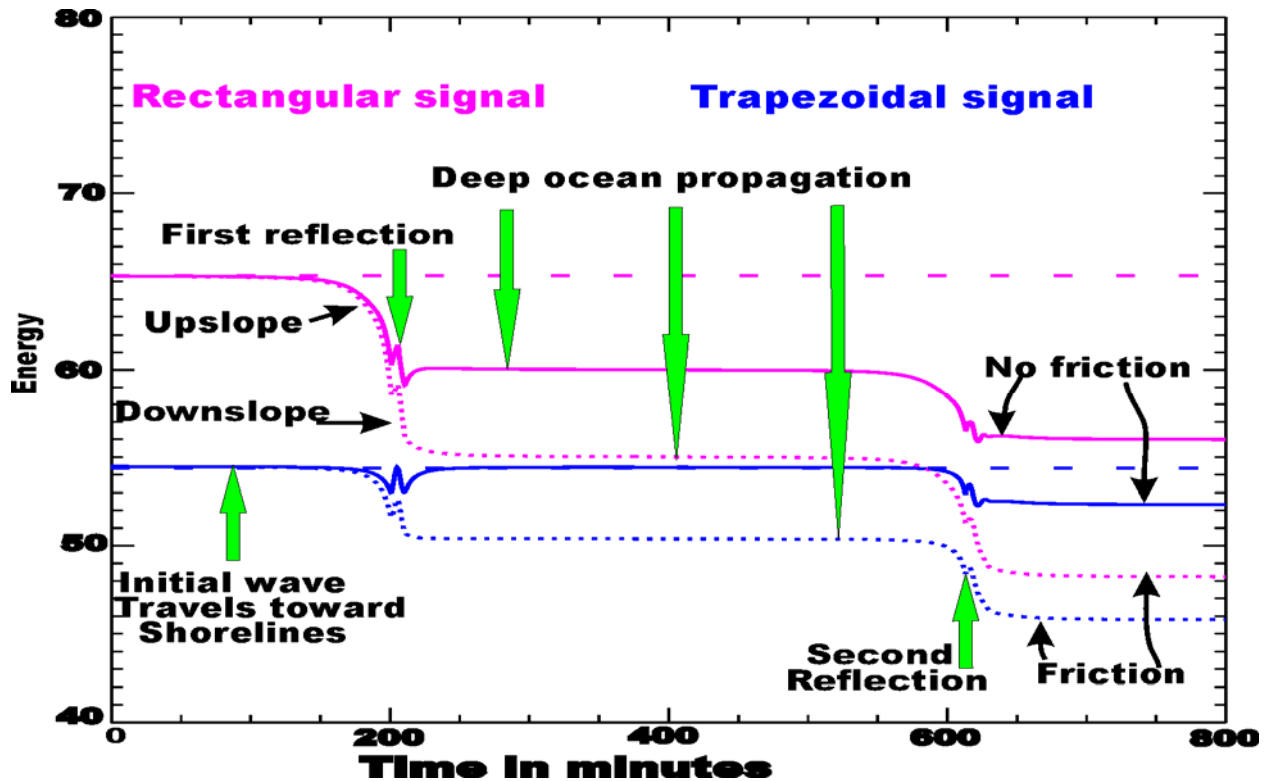


Figure 18. Total energy (kinetic and potential) averaged over computational domain.

The total energy as a function of time has been plotted in Fig. 18. As signal enters the shallow water domain it starts to lose energy both in case when the bottom friction term is included (dotted lines) and when the bottom friction term is set to zero (continuous lines). The latter result confirms the energy dissipation due to the spatial and temporal resolution of the numerical schemes.

In our computations the nonlinear advective term has been rendered into a numerical form through the upstream/downstream method, therefore to explain the energy loss we can invoke numerical friction due to the first order of approximation. For this purpose in eq. (1) only advection along the x direction is considered

$$\frac{\partial u}{\partial t} + u \frac{\partial u}{\partial x} = 0.$$

Its numerical form is

$$\frac{u_j^{m+1} - u_j^m}{T} + u_{j,p}^m \frac{u_j^m - u_{j-1}^m}{h_x} = 0 \quad (8)$$

Here: m is the time stepping index, T is the time step, j the spatial index, h_x is the space step.

The formula above has been written for the positive velocity $u_{j,p}^m$ only. It can be linearized by considering $u_{j,p}^m$ as the constant coefficient. The numerical error introduced by spatial and temporal approximations in (8) is expressed by the second derivative (Kowalik and Murty, 1993, p. 53), as

$$\frac{u_{j,p}^m h_x}{2} \frac{\partial^2 u^m}{\partial x^2}$$

(9)

This numerical term is actually similar to the horizontal friction with viscosity coefficient being a function of the space step h_x and velocity $u_{j,p}^m$. Such numerical viscosity coefficient, because of its dependence on the velocity, produces the strongest dissipation in the shallow water region. Unfortunately, this numerical viscosity coefficient does not explain the deep-water dissipative processes, as the deep-water velocity is very small.

Spectral properties of the numerical dissipation can be further elucidated by considering an amplification which numerical scheme introduces to the unit amplitude sinusoidal signal when computation are advanced from the time step m to $m+1$. If again, eq.(8) can be considered as a linear equation with coefficient $u_{j,p}^m$, an amplification factor (λ) is calculated as (Kowalik and Murty, 1993, p. 46),

$$\lambda = \sqrt{[1 + 2q(q-1)(1-a)]} \quad (10)$$

Here $q = u_{j,p}^m T / h_x$ is the Courant number and $a = \cos \kappa h_x$. The latter parameter defines spatial resolution of a wave length L through the wave number $\kappa = 2\pi / L$. The shortest wave in the system is equal to $2h_x$. Obviously eq.(10) defines the signal amplification as a function of two dimensionless parameters q and a .

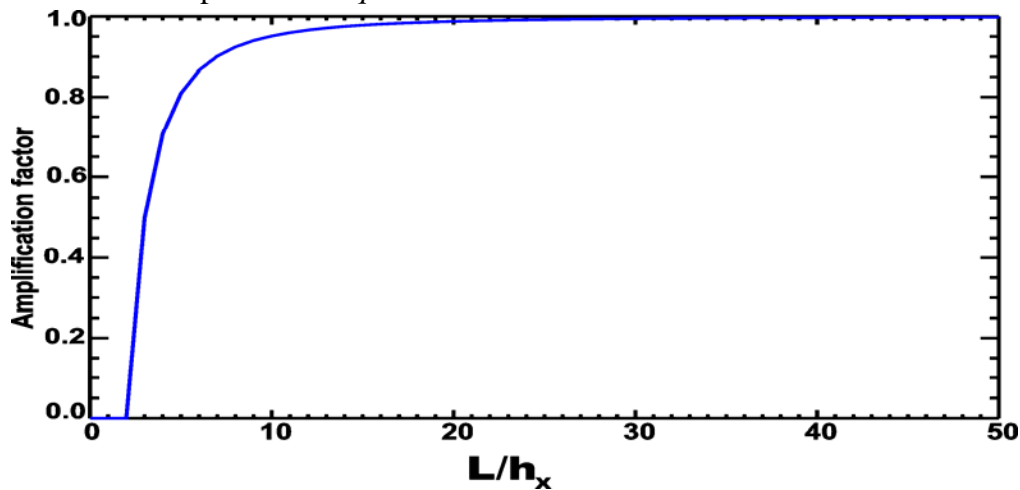


Figure 19. Amplification factor (λ) for the numerical scheme given by eq.(8) as a function of wavelength resolution. L denotes the wavelength, h_x is the space step.

We intend to demonstrate that in the numerical scheme given by eq.(8) the amplification factor suppresses short waves, thus dissipation of energy will take place in the short wave range. For the longer waves when $\kappa \rightarrow 0$ the damping will be negligible. Fig. 19 shows λ as a function of the wave number. In this figure, the Courant number is $q=0.5$. Argument of the cosine function $\kappa h_x = \frac{2\pi}{L} h_x$ defines how well is the wavelength resolved by the spatial step. It changes as a function of the wavelength, starting from the shortest wave $L = 2h_x$, $\kappa h_x = \frac{2\pi}{2h_x} h_x = \pi$ and continues increasing towards the longer waves as shown in Fig. 19. The amplitude of the shortest wave $L = 2h_x$ is completely suppressed in this numerical system. Even if the wavelength is resolved ten times $L/h_x = 10$, the amplification factor is equal $\lambda = 0.95$. The wave described by the rectangular sea level change (Fig. 16) consists of multiple short waves; therefore the numerical scheme will quickly dissipate the short wave energy. The total energy in the near shore region in Fig. 18 depicts a small kink as the wave reflects from the shore. The wave energy instead of being dissipated is growing in this region, thus pointing towards instabilities of the numerical scheme (Phillips, 1959). The source of this energy is not related to physics but to numerics. As eq.(8) is not completely linear, the nonlinear effects will grow in the shallow water due to the sea level and velocity enhancement. A numerical nonlinear instability usually starts at the shortest wavelength in the system since a cascade of motion which arrives from the large scales to the small scales is blocked by the lack of finer resolution. The result is the build up of energy at the short wavelengths which induces instability. Often this type of instability is referred to as aliasing, which points out to the fact that the finite numerical grid cannot discern certain wavelength (see Roache, 1976, p. 81). An example how the new wavelength can be generated through the nonlinear interaction has been given by Kowalik and Murty (1993, p. 179).

Acknowledgment

I would like to express my deep gratitude to George Pararas-Carayannis, President of Tsunami Society, Juan Horillo, University of Alaska Fairbanks and William Knight, West Coast/Alaska Tsunami Warning Center for their comments and suggestions which enhanced this manuscript.

References:

- Candella, R. N., A. B. Rabinovich and R. E. Thomson. 2008. The 2004 Sumatra tsunami as recorded on the Atlantic coast of South America. *Adv. Geosci.*, 14, 117–128.
- Davies, T. A., P. Wilde and D. A. Clague . 1972. Koko Seamount: A major guyot at the southern end of the Emperor Seamounts, *Mar. Geol.*, 13, 311--321.
- Fujima, K., Y. Dede, Goto, C. Hayashi, K., Shigemura, T. 1995. Characteristics of long waves trapped by conical island. *Coastal Engineering Journal*, 38(2), 111-132
- Henry, R. F. and M. G. G. Foreman, 2001. A representation of tidal currents based on energy flux, *Marine Geodesy*, 24(3), 139-152.
- Hirata, K., K. Satake, Y. Tanioka, T. Kuragano, Y. Hasegawa, Y. Hayashi, and N. Hamada. 2005. The Indian Ocean Tsunami: Tsunami Source Model From Satellite Altimetry. *Proceedings of the International Tsunami Symposium*, eds., G.A. Papadopoulos and K. Satake, Chania Greece, 2005, 72-76.
- Horrillo, J., W. Knight, and Z. Kowalik. 2008. Kuril Islands tsunami of November 2006: 2. Impact at Crescent City by local enhancement, *J. Geophys. Res.*, 113, C01021, doi:10.1029/2007JC004404.
- Imamura, F.: 1996, Review of tsunami simulation with a finite difference method. In *Long-Wave Run-up Models*, H. Yeah, P. Liu and C. Synolakis, Eds, World Scientific, 25-42.
- Kajiura, K.. 1981. Tsunami energy in relation to parameters of the earthquake fault model. *Bull. Earthquake Res. Inst.*, 56,415-440.
- Koshimura, S., Y. Hayashi, K. Munemoto and F. Imamura. 2008. Effect of the Emperor seamounts on trans-oceanic propagation of the 2006 Kuril Island earthquake tsunami. *Geophysical Research Letters*, vol. 35, L02611, doi:10.1029/2007GL032129.
- Koshimura, S., F. Imamura, and N. Shuto. 2001. Characteristics of Tsunamis Propagating over Oceanic Ridges, *Natural Hazards*, 24(3), 213–229.
- Kowalik, Z., 2003. Basic relations between tsunamis calculation and their physics-II, *Science of Tsunami Hazards*, 21(3), 154-173.
- Kowalik, Z., J. Horrillo, W. Knight, and T. Logan. 2008. Kuril Islands tsunami of November 2006: 1. Impact at Crescent City by distant scattering, *J. Geophys. Res.*, 113, C01020, doi:10.1029/2007JC004402.
- Kowalik, Z., Knight, W. Logan, T. and P. Whitmore, 2007a. The tsunami of 26 December 2004: Numerical Modeling and energy considerations-II. In: *Tsunami and Its Hazard in Pacific and Indian Oceans*, Eds: Satake, K., Okal, E. A., Borrero, J. C., *Pure and Applied Geophysics (PAGEOPH)*, vol. 164, No. 2/3, 379-393.
- Kowalik Z., W. Knight, T. Logan, and P. Whitmore. 2007b. Numerical Modeling of the Indian Ocean Tsunami. In: *The Indian Ocean Tsunami*. Co-editors: T. Murty, U. Aswathanarayana and N. Nirupama. Taylor and Francis, London, pp. 97-122.
- Kowalik Z., W. Knight, T. Logan, and P. Whitmore, 2005a. Numerical Modeling of the Global Tsunami: Indonesian Tsunami of 26 December 2004. *Science of Tsunami Hazards*, Vol. 23, No. 1, 40- 56.
- Kowalik, Z., Knight, W. Logan, T. and P. Whitmore, 2005b. The tsunami of 26 December 2004: Numerical Modeling and energy considerations, *Proceedings of the International Tsunami Symposium*, Eds.: G.A. Papadopoulos and K. Satake, Chania, Greece, 27-29 June, 2005, 140-150.

- Kowalik, Z. and T. S. Murty. 1993. Numerical Modeling of Ocean Dynamics. World Scientific Publ., 481 pp.
- Kurkin, A., and E. Pelinovsky. 2002. Focusing of edge waves above a sloping beach, *European Journal of Mechanics B/Fluids* 21, 561–577
- Lautenbacher, C. C. 1970. Gravity wave refraction by islands. *J. Fluid Mech.* 41, 655-672.
- Lay, T., H. Kanamori, C. J. Ammon, M. Nettles, S. N. Ward, R. C. Aster, S. L. Beck, S. L. Bilek, M. R. Brudzinski, R. Butler, H. R. DeShon, G. Ekstrom, K. Satake, S. Sipkin. 2005. The Great Sumatra-Andaman Earthquake of 26 December 2004. *Science*, v. 308, 1127-1139.
- Liu PLF, Cho YS, Briggs MJ, Kanoglu U, Synolakis CE. 1995. Runup of solitary wave on a circular island. *Journal of Fluid Mechanics.* 302:259-285.
- Longuet-Higgins, M.S. 1967. On the Trapping of Wave Energy Round Islands. *Jour. Fluid Mech.*, Vol. 29, Part 4, pp 781-821.
- Loomis, H. G. 1966. Spectral analysis of tsunami records from stations in the Hawaiian Islands, *Bull. Seismol. Soc. Am.*, 56, 697– 713.
- Lynett, P. J., T.-R. Wu and P.L.-F.Liu. 2002. Modeling wave run-up with depth-integrated equations, *Coast. Engrg.* 46(2), 89-107.
- Mader, C. L.: 2004, *Numerical Modeling of Water Waves*, CRC Press, 274 pp.
- Mei, C. C.: 1989, *The Applied Dynamics of Ocean Surface Waves*, World Scientific, 740 pp.
- Merrifield, M.A., Y.L. Firing, G. Brundrit, R. Farre, B. Kilonsky, W. Knight, L. Kong, C. Magori, P. Manurung, W. Mitchell, F. Shillington, E.M.S. Wijeratne, J. Jardin, S. Nakahara, F.-Y. Porter, and N. Turesky. 2005. Tide Gauge Observations of the Indian Ocean Tsunami, December 26, *Geophysical Research Letters.* 32, , L09603, doi:10.1029/2005GL022610.
- Mofjeld, H.O., V.V. Titov, F.I. Gonzalez, and J.C. Newman. 2000. Analytic Theory of Tsunami Wave Scattering in the Open Ocean with Application to the North Pacific. NOAA Technical Memorandum OAR PMEL-116, 42pp.
- Munger S. and K. F. Cheung. 2008. Resonance in Hawaii waters from the 2006 Kuril Islands Tsunami. *Geophysical Research Letters*, 35, L07605, doi:10.1029/2007 GL032843.
- Munk, W.H. 1963. Some Comments Regarding Diffusion and Absorption of Tsunamis. In *Proc. Tsunami Meetings Associated with the Tenth Pacific Science Congress*, Honolulu, Hawaii, Aug.- Sept. 1961, ed. Doak C. Cox, IUGG, Paris, IUGG Monograph No. 24, pp 53-72.
- Munk, W., F. Snodgrass, and G. Carrier. 1956. Edge waves on the continental shelf, *Science*, 123(3187), 127– 132.
- Murty, T.S., 1977. Seismic Sea Waves - Tsunamis, Bulletin 198, Fisheries Research Board of Canada, Dept. of Fisheries, Ottawa, Canada, 337 pp.
- Murty, T., Rao, A.D, Nirupama, N., and Nistor, I. and. (2006). Tsunami warning systems for the hyperbolic (Pacific), parabolic (Atlantic) and elliptic (Indian) oceans, *J. of Ind. Geophysical Union.*, Vol. 10, No. 2, 69-78.
- Nekrasov, A. V. 1970. Transformation of tsunamis on the continental shelf. In: *Tsunamis in the Pacific Ocean*, W.M. Adams, ed, East_West Center Press, Honolulu, 337-350.
- Nekrasov, A. V. 1992. On tidal energy horizontal circulation. *The Journal of the Korean Society of Coastal and Ocean Engineers*, 4(3), 168--177.
- Nirupama, N., T.S. Murty, I. Nistor and A.D. Rao. 2006. Persistent high water levels around Andaman & Nicobar Islands following the 26 December 2004 Tsunami, *Science of Tsunami Hazards*, Vol. 24, No. 3, 183-193.

- Phillips, N. A. 1959. An example of Non-Linear Computational Instability. *The Atmosphere and the Sea in Motion*, The Rockefeller Institute Press, New York, N.Y., pp. 501-504.
- Rabinovich, A. B. 1997. Spectral analysis of tsunami waves: Separation of source and topography effects, *J. Geophys. Res.*, 102, 12,663– 12,676.
- Rabinovich A.B., R.E. Thomson and F.E. Stephenson. 2006. The Sumatra tsunami of 26 December 2004 as observed in the North Pacific and North Atlantic oceans, *Surv. Geophys.*, 27, 647–677.
- Roache, P. J. 1976. *Computational Fluid Dynamics*. Hermosa Publishers, 446 pp.
- Titov, V., A. B. Rabinovich, H. O. Mofjeld, R. E. Thomson and F. I.Gonzales. 2005. The Global Reach of the 26 December 2004 Sumatra Tsunami, *Science*, 309, 2045–2048.
- Van Dorn W. G. 1970. Tsunami Response at Wake Island: a Model Study. 1970. *Journal of Marine Research*, v.28, no.3, 336-344.
- Van Dorn, W.G. 1984. Some Tsunami Characteristics Deducible from Tide Records. *Jour. Physical Oceanography*, Vol. 14, No. 2, 353-363.
- Yanuma, T., and Y. Tsuji. 1998. Observation of edge waves trapped on the continental shelf in the vicinity of Makurazaki Harbor, Kyushu, Japan, *J. Oceanogr.*, 54, 9– 18.